Hindawi

*Research Article*

# Progressive Collapse Resistance Mechanism of RC Frame Structure Considering Reinforcement Corrosion

**Chao Bao** [ID],[1] **Dahai Lv,**[1] **Huxiang Wang,**[1] **Yuhang Zhang,**[1] **Xiaotong Ma,**[2] **Kar Sing Lim,**[3] **and Juping Zhang**[1]

[1]*School of Civil Engineering and Hydraulic Engineering, Ningxia University, Ningxia Hui Autonomous Region, China*
[2]*School of Civil Engineering, North Minzu University, Ningxia Hui Autonomous Region, China*
[3]*Department of Civil Engineering, College of Engineering, Universiti Malaysia Pahang, Pahang, Malaysia*

Correspondence should be addressed to Chao Bao; baochao@nxu.edu.cn

Corrosion causes reduction in cross-sectional area of reinforcement, deterioration of mechanical properties, and degradation of bonding properties between reinforced concrete, which are the most important factors leading to the degradation of structural service performance. In order to investigate the progressive collapse mechanism of a corroded reinforced concrete frame structure, the failure modes, characteristics of the vertical displacement, and load capacity are studied using the finite element method. Based on existing experimental research, the established model is verified, and the influence of different influencing factors on the progressive collapse mechanism is analyzed. The results show that the corrosion of the reinforcement affects the yield load, peak load, and ultimate load of the reinforced concrete substructure. As the corrosion rate increases, the tensile arch action shows a particularly severe deterioration. The variation of concrete strength and the height–span ratio affects the substructure's load-bearing capacity much more significantly than the stirrup spacing.

## 1. Introduction

Progressive collapse of a structure was first proposed after the Ronan Point Apartments incident and is caused by the local failure of a primary load-bearing member under incidental loading, which in turn leads to the partial or disproportionate collapse of the structure, and is also referred to as disproportionate collapse when the damage to the structure causes more damage compared to the source [1, 2]. The British Code gave the first definition of continuous collapse: continuous collapse of a structure means that the initial local damage failure of the structure causes the overall structure to fail out of proportion to the initial damage, resulting in partial or total collapse [3]. While the progressive collapse of structures is a low-probability event, when it occurs, it causes enormous damage to property and threatens lives, spurring public outrage, and causing widespread concern worldwide. Therefore, it is necessary to study the progressive collapse of structures. Since the collapse of

the Roman Point Apartments in 1968, the Alfred P. Murrah Federal Building in the United States and the World Trade Center in New York in 2001, a new era in the study of progressive collapse has begun, and a large number of experts have focused on the study of the resistance of structures to progressive collapse. A large number of studies have been carried out on reinforced concrete (RC) frames, and a number of research results have been obtained. Investigation of the mechanisms behind progressive collapse resistance of RC frame structures has been carried out around the world, and the relevant methods mainly include experimental studies, numerical analysis, and theoretical studies. Xi et al. [4] studied the stress distribution and load transfer characteristics of the compressive arch action (CAA) of concrete beam–column members under middle column removal using experiments and numerical simulation and derived a theoretical calculation formula considering the bending deformation and axial deformation of the arch. Yu and Tan [5] investigated the influence of different axial constraints, different

reinforcement ratios, and different span–depth ratios on the structural performance through quasi-static force experiments and studied the alternative load path to reduce progressive collapse by proposing a deformation judgment to achieve the CAA. Alshaikh et al. [6] proposed a test study on one-third scale in the removal scenario of the middle column to investigate the inclusion efficiency of straight microsteel fibers to improve the structural ductility and deformability of RC frames to achieve progressive collapse resistance. Wang et al. [7] experimentally studied the effect of assembled tensile steel brace on the progressive collapse resistance of concrete-filled steel tubular and found that the horizontal reaction forces of the specimens were compressive forces due to the CAA in the initial loading stage, and they changed from compression to tension due to the catenary action. Wang et al. [8] experimentally studied the load carrying mechanisms in resisting progressive collapse for RC structures while considering transverse beam and slab effects, and the result showed that the risk of progressive collapse could be mitigated by the transverse beam and slab. Kiran et al. [9] studied the pull out behavior of reinforcement steel exposed to standard fire exposure and found a drastic reduction in bond strength of concrete and tensile strength of the rebar while increasing the duration of heating. Li et al. [10] experimentally evaluated the development of the structural temperature field and horizontal restraint force under simulated fire conditions as well as the mode of cracking due to cooling, and then, this work also focused on the effect of different rebar arrangements and different post-fire conditions on the resistance of the structure to progressive collapse. Zhang and Li [11] experimentally investigated the contribution of floor slabs to the resistance of the structure to progressive collapse and investigated the effect of various parameters on the progressive collapse possibility of RC frame structures by finite element method (FEM). Qian et al. [12] investigated the effect of reinforcement corrosion on the progressive collapse resistance mechanism of frame structures by rusting the nodal region of the substructure and found that reinforcement corrosion reduces the yield strength, peak load, and ultimate load capacity of the substructure, weakens the contribution of CAA and TCA to the resistance to progressive collapse resistance, and changes the fracture location of the reinforcement and the sequence of crack development.

Due to the large amount of financial and human resources spent on experiments and the limitations of these various experimental conditions, a large number of researchers have investigated the effects of different parameters on the resistance of structures to progressive collapse using FEM. Feng et al. [13] explored the progressive collapse behavior of precast RC frame members and investigated the effect of typical parameters on the structure by building a FE model. Alshaikh et al. [14] used FEM and found that the rubber concrete beam–slab substructure performed well in tensile catenary action (TCA) with additional resilience to significant deformation. Qian et al. [15] built a macroscopic finite element model of an RC slab frame. The results showed that the inclusion of cladding and infill walls could improve the ultimate load and initial stiffness, and the infill walls changed the load path of the frame and improved the

load distribution capacity of the frame. Li et al. [16] established complete RC frames by FEM to investigate the effect of column failure at different typical locations on different floors on each mechanism of resistance to progressive collapse. Li et al. [17] investigated the resistance to progressive collapse of prestressed precast concrete frame structures by establishing a FE model and proposed a method for calculating the resistance to collapse of prestressed PC frame structures in CAA. Chang et al. [18] established a FE model of prestressed concrete frame with infill wall and found that the infill wall can enable the structure to enter TCA in advance, improving the collapse resistance bearing capacity of the prestressed concrete frame. Studies by Yu et al. [19] showed that the progressive collapse resistance of the RC beam–slab substructure is mainly attributed to the compression arch action of the beam, the bending mechanism, the TCA, and the tensile membrane action of the slab. Kakhki et al. [20] established a FE model to investigate the relationship between the frame structure and parameters such as soil density, soil type, soil layer, and soil saturation conditions. Pang et al. [21] studied the influence of the arrangement form of reinforcement and reinforcement methods on the progressive collapse resistance of infilled RC frame and proposed a semi-analytical model for predicting the post-loss load capacity of infilled frame columns. Xu et al. [22] established a FE model of RC frame structures with masonry infill walls based on FEM to study the effects of different scaled distance blast loads, different column damage locations, and different span numbers on the structural performance. Zhang et al. [23] investigated the variation of CAA and TCA as the corrosion of reinforcement increases over a period of 0 ~ 70 years by means of a finite element numerical simulation method, based on the verification of the correctness of the finite element analysis. The numerical model is capable and feasible for the prediction of the progressive collapse resistance of reinforcement corrosion structures. Feng et al. [24] used the probabilistic density evolution method to calculate the reliability index of the structure, and established a finite element analysis model by considering the degradation of the bond between reinforcement and concrete, and the deterioration of the material properties of reinforcement and concrete, and found that reinforcement corrosion has a large impact on the collapse resistance and ductility of the structure, and the rate of degradation slows down after 30 years. Finally, the effect of different influencing factors on the progressive collapse resistance of the structure is investigated.

However, most of the existing studies on structural resistance to progressive collapse have ignored the problems of loss of structural durability and degradation of serviceability. Considering the common chloride salt erosion problem as an example, the erosion of a structure by chloride salt causes a reduction in the cross-section of the reinforcement and a decrease in its strength and ductility. Then, following expansion of the corrosion products, the corrosion products grow to four to six times their initial volume [25], which will cause the expansion and cracking of the concrete cover. This not only reduces the ability of the reinforcement and concrete to share loads but also seriously reduces the service life and

overall performance of the structure. Rarely have researchers exclusively investigated the degradation caused by corrosion of the reinforcement at the nodes. For the long-term service structures especially in corrosive environments, existing research results still have difficulty revealing the influence trend of performance degradation during service on the performance of progressive structural collapse, and there remains a lack of robust research results to support this consideration. Therefore, in this study, an RC frame beam–column substructure model is established by FEM to reveal the influence mechanisms of various parameters on the RC frame substructure during transformation and loading.

## 2. Method

With sufficient lateral restraint, if a vertical member fails, the collapse resistance of the structure is mainly provided by the beam, with CAA provided by the top beam of the failed column and TCA in the large deformation stage resisting progressive collapse.

*2.1. Specimen Design.* Three reference specimens [12] are used as examples. The clear span of the substructure beam is 2000 mm, the total length is 5050 mm, the stressed longitudinal reinforcement is HRB400, and the stirrup is HPB335. The substructure consists of three short columns and two span beams. The upper part of the beam is equipped with two 12 mm diameter full-length reinforcements and one 12 mm diameter truncated reinforcement, and the lower part of the beam is equipped with two 12 mm diameter full-length reinforcements. During the experiment, the vertical load is applied directly to the top of the central column to simulate failure of this column. The reinforcement of the substructure is shown in Figure 1.

The specimen in literature [12] is used as an example. The substructure specimen BS-0 beam has a net span of 2000 mm, a total length of 5050 mm, the stressed longitudinal reinforcement is HRB400, and the stirrup is HPB335. The substructure consists of three short columns and two span beams. The upper part of the beam is equipped with two 12 mm diameter full-length reinforcements and one 12 mm diameter truncated reinforcement, and the lower part of the beam is equipped with two 12 mm diameter full-length reinforcements. During the experiment, vertical load is directly applied to the top of the middle column to simulate the failure condition of the middle column. The concrete reinforcement of the substructure specimens BS-0 is shown in Figure 1, and the beam and column cross-sectional dimensions and reinforcement of the specimen BS-15-5 and BS-30-5 are the same as those of the specimen BS-0.

*2.2. Numerical Modeling.* The model uses the hexahedral reduced solid unit C3D8R for the concrete and the three-dimensional two-node truss unit T3D2 for the reinforcement. The mesh size of the model directly determines the calculation efficiency and calculation time of the model, and it is found that when the mesh size of the model is less than 75 mm, it is found that the calculation result is less than 75 mm. Therefore, based on the requirements of computational efficiency and accuracy, this paper selects a hexahedral mesh with a cell size between 25 and 50 mm. Figure 2 shows the 3D model diagram and force schematic of the finite element model. The model does not take into account the bond–slip effect between the stirrup and the concrete, and the stirrup is embedded in the concrete using the EMBED command. Three perpendicular nonlinear spring elements are inserted between the stressed longitudinal reinforcement and the concrete to simulate the bond–slip effect between the reinforcement and the concrete. The nonlinear springs cannot be added directly in ABAQUS/CAE and are therefore modified into the INP file. When modifying the INP file, it should be noted that the displacements must be arranged in ascending order, these displacements must be larger to ensure the correctness of the definition, and the coincidence of the steel and concrete nodes should be taken into account when defining the spring units.

The model simulates the boundary conditions with the simplification of not considering the influence of the steel plates and bolts used for fixing. The upper and lower interfaces of the side columns are completely fixed. The model uses displacement control to apply a concentrated load, and the point of application is the coupling point on the upper surface of the middle column, in accordance with the experimental load applications. This signifies that the model is constrained out of the plane, so that it can only move vertically to prevent the structure from becoming laterally deformed.

*2.3. Material Properties.* In the model, the nonlinear behavior of concrete is simulated by the plastic damage Concrete Damaged Plasticity model, the concrete strength is taken from literature [12], and the cubic compressive strength and elastic modulus of concrete are 43.1 MPa and $3.33 \times 10^4$ MPa, respectively. The main stress–strain relationship equation [26] for concrete is given below, and the main relationship curve is shown in Figure 3(a).

The stress–strain constitutive equation of concrete under uniaxial tension is:

$$\sigma_c = \begin{cases} E_c \varepsilon_0 & \varepsilon \leq \varepsilon_0 \\ (1 - d_t) E_c \varepsilon_c & \varepsilon_0 \leq \varepsilon_c \leq \varepsilon_{cu} \end{cases}, \tag{1}$$

$$d_t = \begin{cases} 1 - \rho_t \left[ 1.2 - 0.2 x^5 \right] & x \leq 1 \\ 1 - \dfrac{\rho_t}{\alpha_t (x - 1)^{1.7} + x} & x > 1 \end{cases}, \tag{2}$$

where $\alpha_t$ is the parameter values of the falling section of the uniaxial tensile stress–strain curve of concrete; $f_t$ is the representative values of uniaxial tensile strength of concrete; $\varepsilon_t$ is the peak tensile strain of concrete corresponding to the representative value of uniaxial tensile strength of concrete; and $d_t$ is the concrete uniaxial tensile damage evolution coefficient parameters.
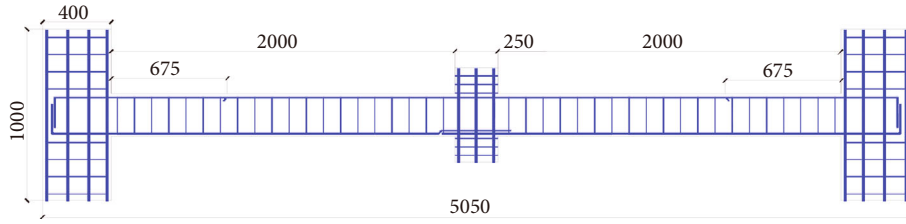
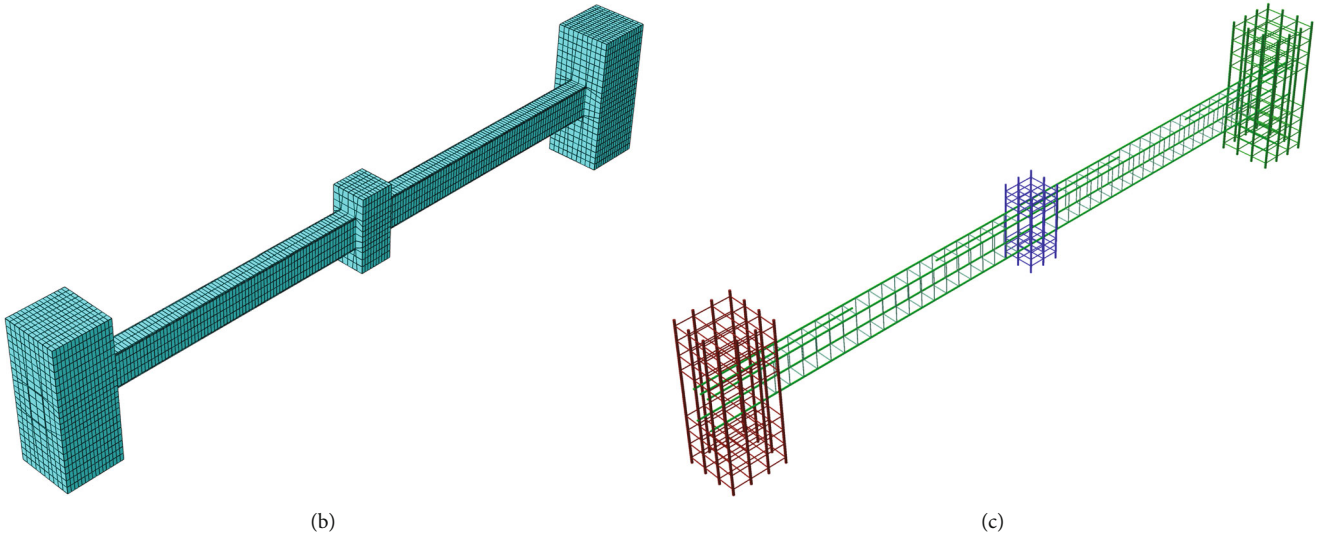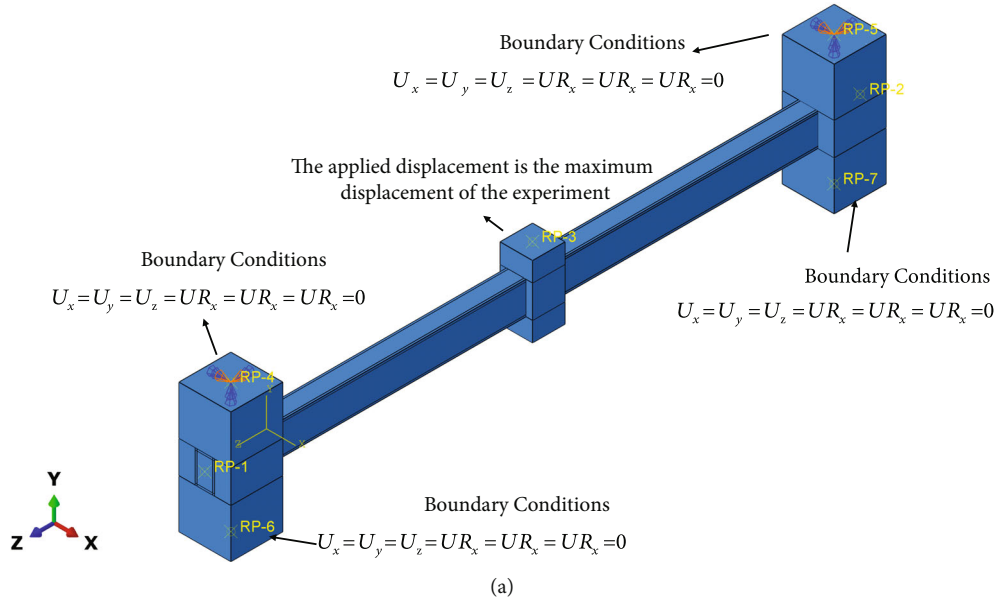FIGURE 1: Substructure rebar diagram.



(a)



(b)



(c)

FIGURE 2: FE model. (a) Boundary conditions of the model and applied loads. (b) FE model cell meshing. (c) Steel reinforcement cage.

The stress–strain constitutive equation of concrete under uniaxial tension is:

$$\sigma_c = \begin{cases} E_c \varepsilon_0 & \varepsilon \leq \varepsilon_0 \\ (1 - d_c) E_c \varepsilon_c & \varepsilon_0 \leq \varepsilon_c \leq \varepsilon_{cu} \end{cases}, \qquad (3)$$

$$d_c = \begin{cases} 1 - \dfrac{\rho_c n}{n - 1 + x^n} & x \leq 1 \\ 1 - \dfrac{\rho_c}{\alpha_c (x - 1)^2 + x} & x > 1 \end{cases}, \qquad (4)$$

where $\alpha_c$ is the values of parameters of the falling section of the uniaxial compressive stress–strain curve of concrete; $f_c$ is
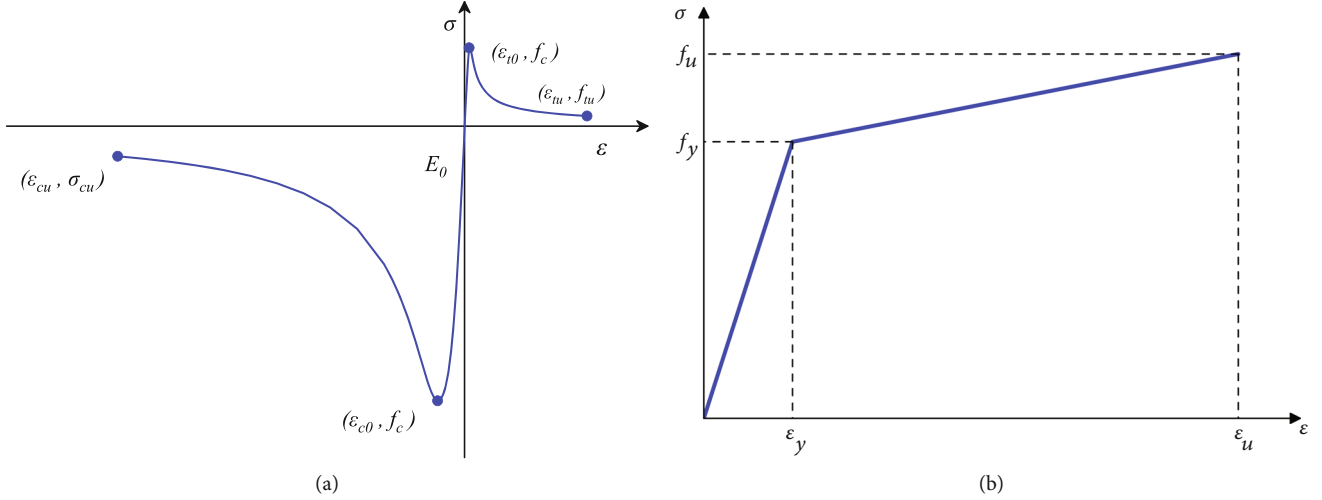
FIGURE 3: Material constitutive relation curve. (a) Concrete principal structure relationship curve. (b) Rebar principal structure relationship curve.

TABLE 1: Material properties of steel reinforcement.

| Corrosion rate $\eta$/% | Diameter of steel bar/ mm | Yield strength $f_y$/MPa | Ultimate strength $f_u$/ MPa | Elongation $\delta$/% |
|---|---|---|---|---|
| 0 | 6 | 348 | 486 | 25.4 |
|  | 12 | 438 | 577 | 16.6 |
|  | 16 | 466 | 605 | 16 |
| 4.8 | 6 | 324 | 453 |  |
|  | 12 | 408 | 538 | 15.1 |
| 10 | 6 | 296 | 413 |  |
|  | 12 | 373 | 490 | 13.15 |
| 4.2 | 6 | 270 | 376 |  |
|  | 12 | 340 | 447 | 11.7 |
| 20 | 6 | 307 | 404 |  |
|  | 12 | 307 | 403 | 9.7 |
| 25 | 6 | 218 | 304 |  |
|  | 12 | 274 | 360 | 7.98 |
| 28.6 | 6 | 192 | 267 |  |
|  | 12 | 250 | 329 | 7.1 |

the representative value of uniaxial compressive strength of concrete; $\varepsilon_c$ is the peak tensile strain of concrete corresponding to the representative value of uniaxial compressive strength of concrete; and $d_c$ is the concrete uniaxial tensile damage evolution coefficient parameters. The values of the relevant parameters were assigned according to the Concrete Design Code (GB50010-2010) [26].

The linear strengthening model was used for the stressed longitudinal bars and hoop reinforcement, and the yield strength and ultimate strength of the longitudinal bars were taken from literature [12], the determination of the mechanical properties of rusted steel bars is determined by intercepting the longitudinal ribs of the column in the crushed

specimen and the bottom longitudinal ribs of the side node beam, and the specific mechanical properties are shown in Table 1.

The constitutive relationship equation of reinforcement is given below, and the constitutive relationship curve is shown in Figure 3(b). The constitutive relationship equation of rebar is:

$$
\begin{cases}
\sigma_s = E_s \varepsilon_s & \varepsilon_s \le \varepsilon_y \\
\sigma_s = f_y + k(\varepsilon_y - \varepsilon_u) & \varepsilon_y < \varepsilon_s < \varepsilon_u , \\
0 & \varepsilon_s \ge \varepsilon_u
\end{cases}
\tag{5}
$$

where $E_s$ is the modulus of elasticity of reinforcement; $\sigma_s$ is the reinforcement stresses; $\varepsilon_s$ is the reinforcement strain; $\sigma_u$ is the value of the stress represented by the ultimate strength of the reinforcement; $\varepsilon_u$ is the strain represented by the ultimate strength of the steel reinforcement; and $k = (f_u - f_y)/(\varepsilon_u - \varepsilon_y)$ represents the slope of the reinforcement section of the steel bar.

Since the ratio of the protective layer thickness to the longitudinal tensile reinforcement in this simulation is less than four, the bond–slip main structure obtained from literature [27] is used for the main structure of the nonlinear spring unit. Moreover, the bond–slip relationship curve is simplified because FEM must present a tradeoff between computational efficiency and accuracy. Since the corrosion of the reinforcement seriously affects the bond relationship between the stressed reinforcement and the concrete, we account for this relationship by introducing the reduction coefficient of the bond strength, as obtained from literature [28] by experimental regression:

$$
\beta = \begin{cases}
1 & \eta_m \le 1.5\% \\
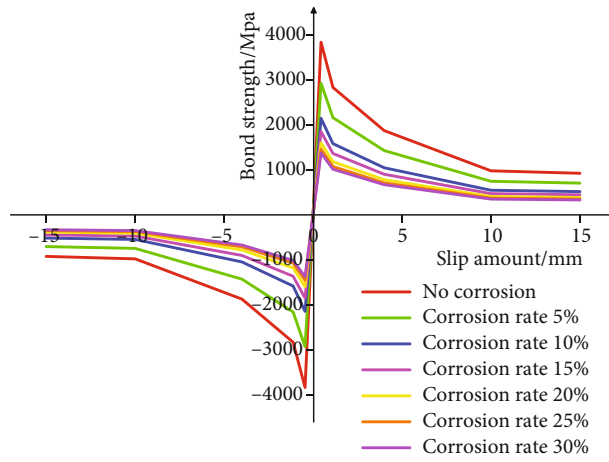e^{-\delta(\eta_m - 1.5\%)} & \eta_m > 1.5\%
\end{cases} .
\tag{6}
$$

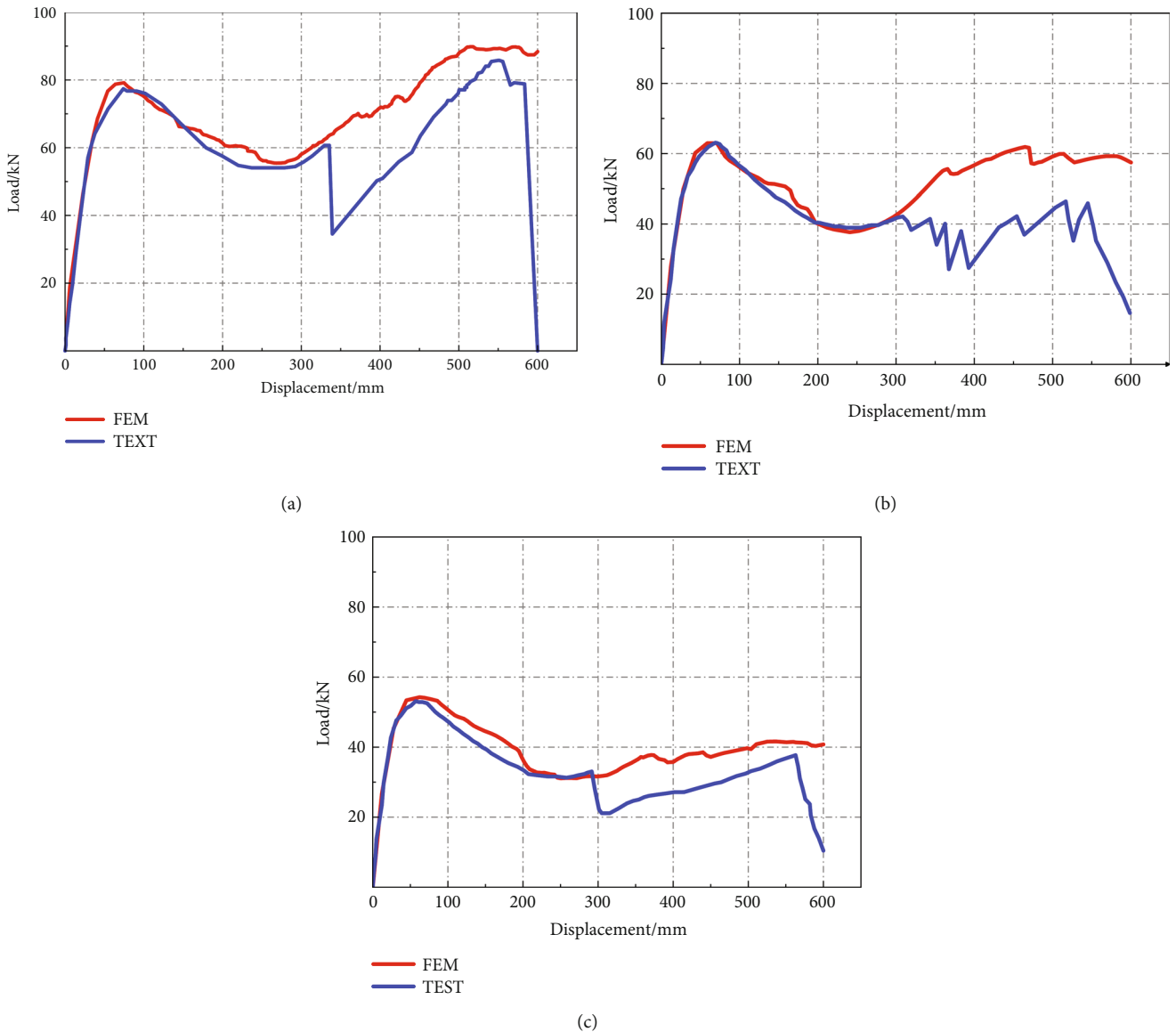Figure 4: Spring force–displacement relationship curve.



(a)



(b)



(c)

Figure 5: Comparison of load–deflection curve relationship between test and FEM. (a) BS-0. (b) BS-15-5. (c) BS-30-5.

TABLE 2: Comparative analysis of the FEM and test results.

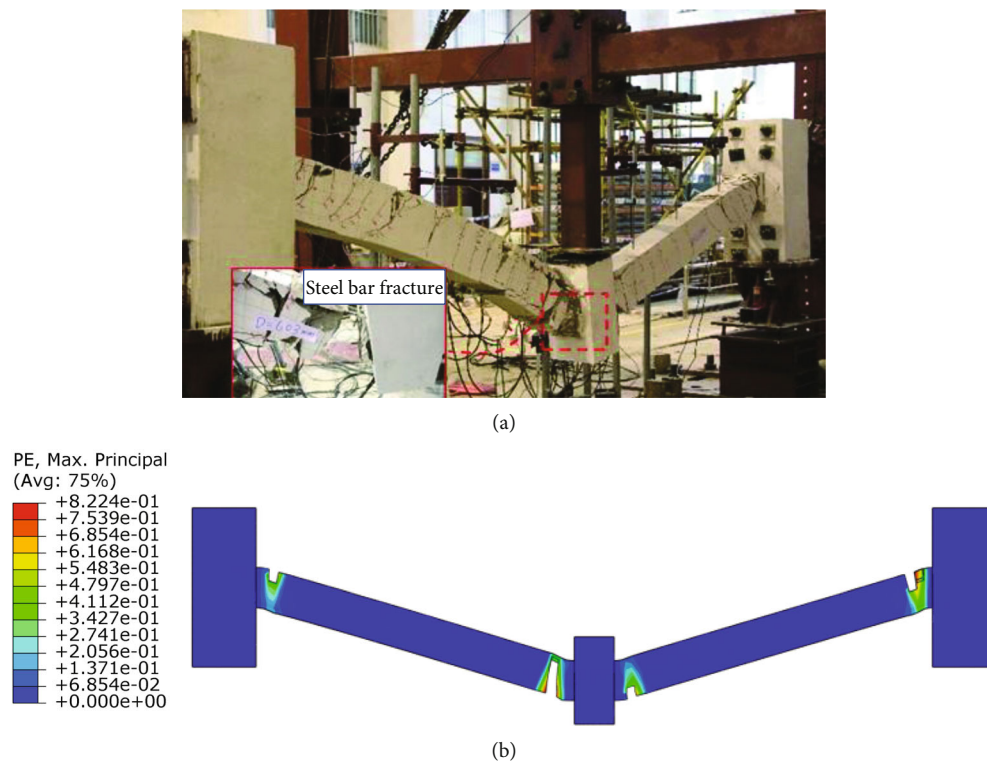| Test number | Yield load $F_y$ (kN) | | Peak load $F_p$ (kN) | | Ultimate load $F_u$ (kN) | | $\frac{F_{y(TEST)}}{F_{y(FEM)}}$ | $\frac{F_{p(TEST)}}{F_{p(FEM)}}$ | $\frac{F_{u(TEST)}}{F_{u(FEM)}}$ |
|---|---|---|---|---|---|---|---|---|---|
| | TEST | FEM | TEST | FEM | TEST | FEM | | | |
| BS-0 | 56 | 57.6 | 77.2 | 77.6 | 88.5 | 89.7 | 0.972 | 0.995 | 0.986 |
| BS-15-5 | 49.1 | 50 | 63 | 61.9 | 45.9 | 58.9 | 0.982 | 1.018 | 0.779 |
| BS-30-5 | 42.8 | 41.7 | 53.1 | 54.1 | 37.7 | 41.6 | 1.023 | 0.982 | 0.906 |
| | | | | | Average value: | | 0.992 | 0.998 | 0.891 |
| | | | | | Standard deviation: | | 0.04 | 0.03 | 0.14 |



(a)



(b)

FIGURE 6: Comparison of BS-0 specimen test crack and FE crack mode. (a) Specimen failure diagram. (b) FE simulation crack diagram.

The mathematical expression for the force–displacement curve of a nonlinear spring cell after corrosion of the steel bar can be written as:

$$F = \beta \tau A_i, \tag{7}$$

where $\tau$ is the bond stress between the reinforcement and the concrete and $A_i$ is the sectional area of the section connected by the spring.

The force–displacement relationship curve of the spring assembly after corrosion is shown in Figure 4. This simulation does not consider the bond between the longitudinal and transverse reinforcement and the concrete, so the spring coefficients of the normal and transverse nonlinear springs take large values, which are generally two orders of magnitude in the longitudinal tangential direction.

2.4. Mechanical Property Degradation Model. Reinforcement corrosion directly reduces the cross-sectional area of the reinforcement, such that the yield strength, ultimate strength, and ductility of the reinforcement are reduced to varying degrees, resulting in a reduction in the load carrying capacity. To determine the change in reinforcement strength, the yield strength, ultimate strength, and elongation are calculated based on reference methods [10]. The cross-sectional area and yield strength of the reinforcement after corrosion can be expressed as:

$$A_{sc} = (1 - \rho_s)A_s, \tag{8}$$

$$f_{yc} = (0.961 - 0.0176\rho_s)f_y, \tag{9}$$

where $A_{sc}$ is the cross-sectional area after corrosion; $A_s$ is the cross-sectional area of the reinforcement without corrosion; and $\rho_s$ is the cross-sectional rust rate.
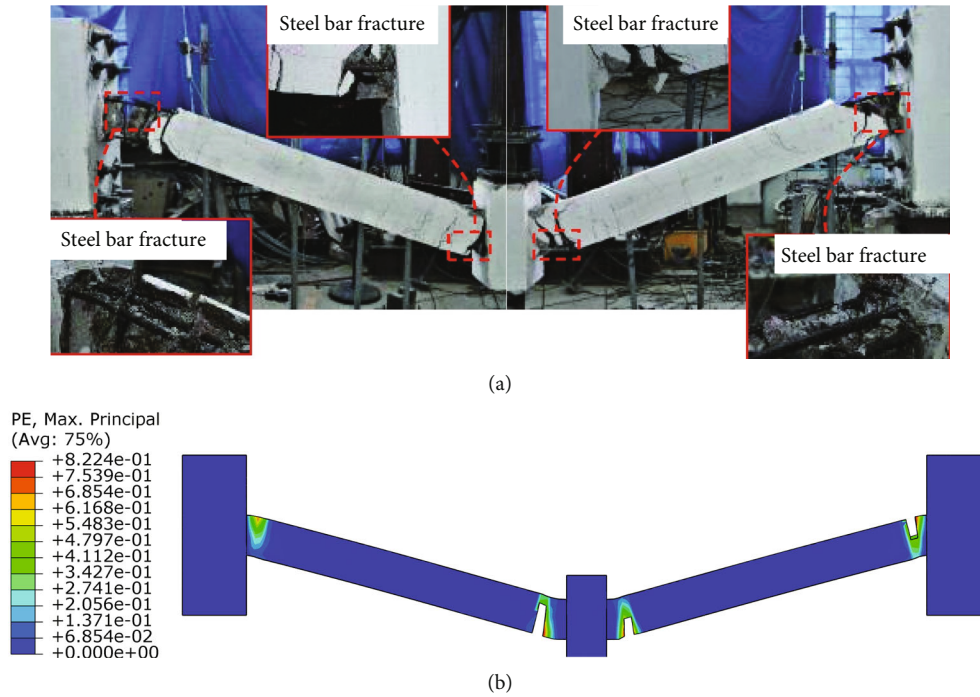
(a)



PE, Max. Principal
(Avg: 75%)
+8.224e-01
+7.539e-01
+6.854e-01
+6.168e-01
+5.483e-01
+4.797e-01
+4.112e-01
+3.427e-01
+2.741e-01
+2.056e-01
+1.371e-01
+6.854e-02
+0.000e+00

(b)

FIGURE 7: Comparison of BS-15-5 specimen test crack and FE crack mode. (a) Specimen failure diagram. (b) FE simulation crack diagram.



(a)



PE, Max. Principal
(Avg: 75%)
+7.422e-01
+6.804e-01
+6.185e-01
+5.567e-01
+4.948e-01
+4.330e-01
+3.711e-01
+3.093e-01
+2.474e-01
+1.856e-01
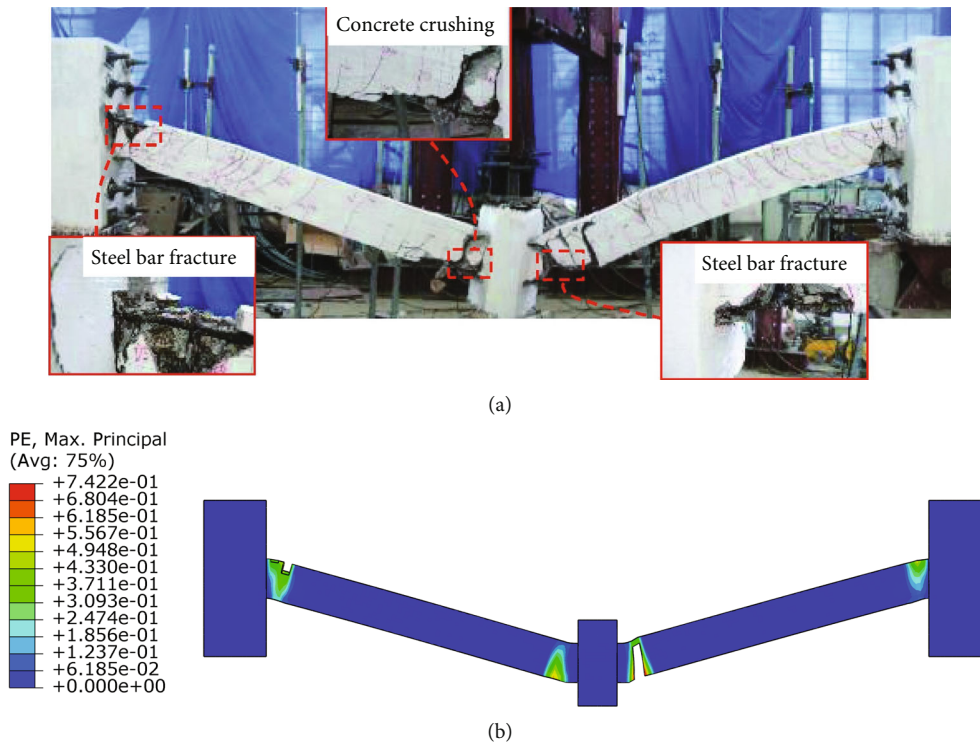+1.237e-01
+6.185e-02
+0.000e+00

(b)

FIGURE 8: Comparison of test crack and FE crack modes of BS-30-5 test piece. (a) Specimen failure diagram. (b) FE simulation crack diagram.
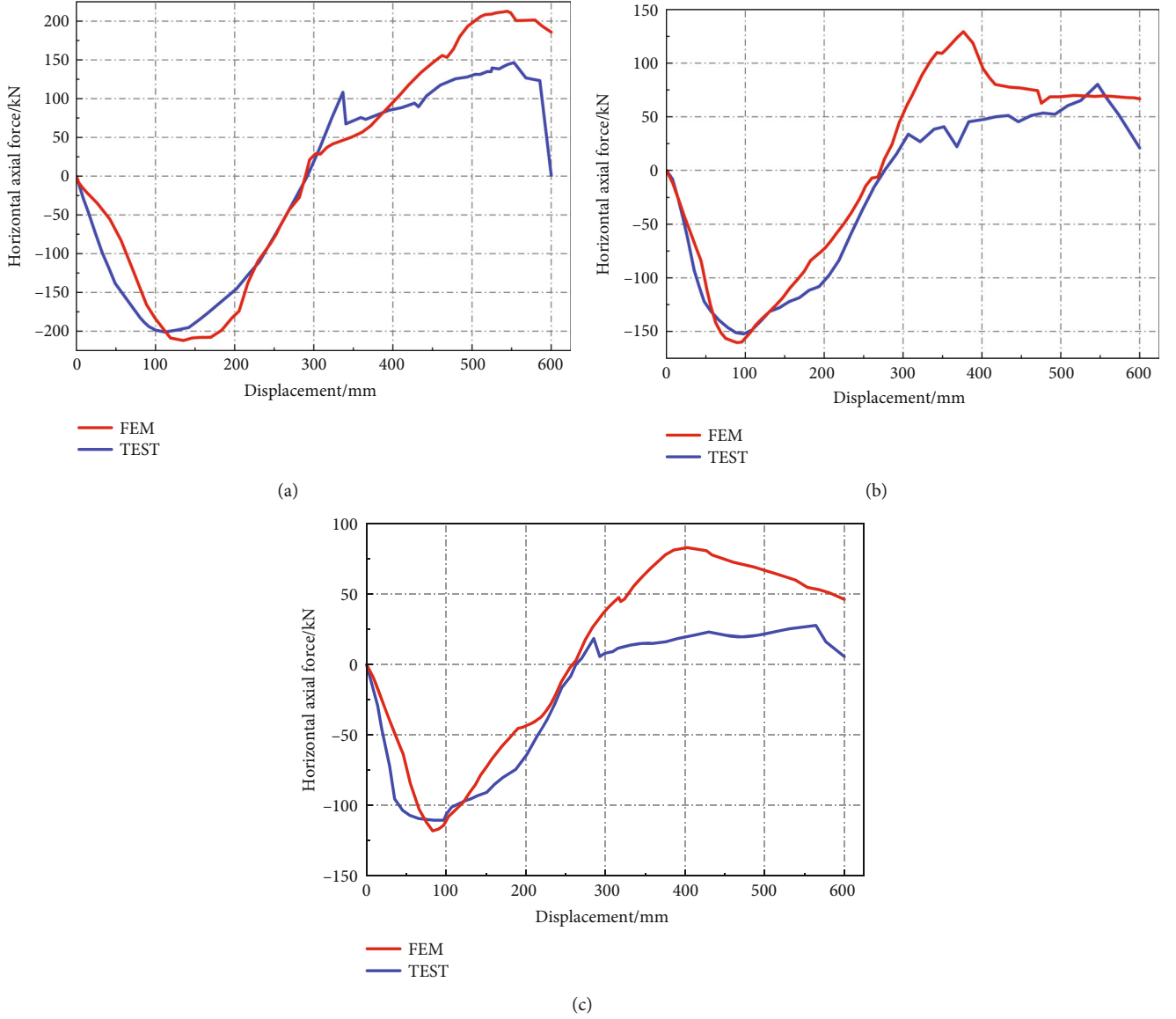
Figure 9: Comparison of horizontal reaction forces between test and FEM. (a) BS-0. (b) BS-15-5. (c) BS-30-5.

The relationship between the volume corrosion rate and the mass corrosion rate can be expressed as [29]:

$$\rho_s = \begin{cases} 0.013 + 0.987\rho & \rho \leq 10\% \\ 0.061 + 0.939\rho & 10\% \leq \rho < 20\% \\ 0.129 + 0.871\rho & 20\% \leq \rho < 30\% \\ 0.199 + 0.801\rho & 30\% \leq \rho < 40\% \end{cases}, \quad (10)$$

where $\rho$ is the quality corrosion rate of the reinforcement.

Because the volume of rebar corrosion products increases to four to six times greater than the initial volumes before corrosion [22], the protective layer of concrete is subjected to tensile forces, the concrete expands and cracks, and these cracks become larger and wider until they fall off and stop working. This leads to a reduction in the cross-sectional area of the concrete and a reduction in the load-bearing capacity. To simulate this performance degradation with the FEM, various methods such as reducing the concrete stressed area and reducing the concrete compressive strength are usually used. It is assumed that there is no reduction in the concrete strength in the core area at the time of reinforcement corrosion. For the concrete protection layer, the concrete strength after corrosion can be calculated using the following equation [30]:

$$f_c^* = \frac{f_c}{1 + K\varepsilon_1/\varepsilon_{co}}, \quad (11)$$

$$\varepsilon_1 = (b_f - b_o)/b_o, \quad (12)$$

$$b_f - b_o = n_{bars}\omega_{cr}, \quad (13)$$

$$\omega_{cr} = \sum_i u_{icorr} = 2\pi(v_{rs} - 1)X, \quad (14)$$

TABLE 3: Comparative analysis of horizontal reactions between FEM and test results.

| Test number | Maximum pressure/kN | | Corresponding displacement/ mm | | Maximum tensile force/kN | | Corresponding displacement/ mm | | Tension pressure conversion point/ mm | |
| --- | --- | --- | --- | --- | --- | --- | --- | --- | --- | --- |
| | TEST | FEM | TEST | FEM | TEST | FEM | TEST | FEM | TEST | FEM |
| BS-0 | 202.0 | 212 | 112 | 135 | 147 | 212.8 | 553 | 544 | 291.8 | 286.0 |
| BS-15-5 | 153.1 | 160.4 | 98.2 | 89.4 | 80.0 | 129.4 | 547 | 376 | 276.5 | 271.4 |
| BS-30-5 | 111.9 | 118 | 84.2 | 83 | 31.0 | 83 | 565 | 402 | 262.0 | 256.3 |

TABLE 4: Specific models under different corrosion rates.

| Influence factor | Specific parameters | Volume corrosion rate% | Model label | Remarks |
| --- | --- | --- | --- | --- |
| Compressive strength of concrete | 30 MPa | 0 | C30-0 | No |
| | | 10 | C30-10 | |
| | | 20 | C30-20 | |
| | | 30 | C30-30 | |
| | 35 MPa | 0 | C35-0 | |
| | | 10 | C35-10 | |
| | | 20 | C35-20 | |
| | | 30 | C35-30 | |
| | 43 MPa | 0 | C43-0 | |
| | | 10 | C43-10 | |
| | | 20 | C43-20 | |
| | | 30 | C43-30 | |
| Stirrup spacing | 50 mm | 0 | S50-0 | No |
| | | 10 | S50-10 | |
| | | 20 | S50-20 | |
| | | 30 | S50-30 | |
| | 100 mm | 0 | S100-0 | |
| | | 10 | S100-10 | |
| | | 20 | S100-20 | |
| | | 30 | S100-30 | |
| | 150 mm | 0 | S150-0 | |
| | | 10 | S150-10 | |
| | | 20 | S150-20 | |
| | | 30 | S150-30 | |
| Height–span ratio | 14 | 0 | H14-0 | Change the span–depth ratio by determining the beam height and changing the beam span. |
| | | 10 | H14-10 | |
| | | 20 | H14-20 | |
| | | 30 | H14-30 | |
| | 16 | 0 | H16-0 | |
| | | 10 | H16-10 | |
| | | 20 | H16-20 | |
| | | 30 | H16-30 | |
| | 18 | 0 | H18-0 | |
| | | 10 | H18-10 | |
| | | 20 | H18-20 | |
| | | 30 | H18-30 | |

where $K$ is the coefficient related to the surface and diameter of the reinforcement (medium diameter ribbed reinforcement can be taken as $K = 0.1$); $\varepsilon_{co}$ is the yield strain; $\varepsilon_1$ is the average strain in the transverse direction of the cracked concrete; $b_0$ is the cross-sectional width of the non-corroded beam; $b_f$ is the effective section width of
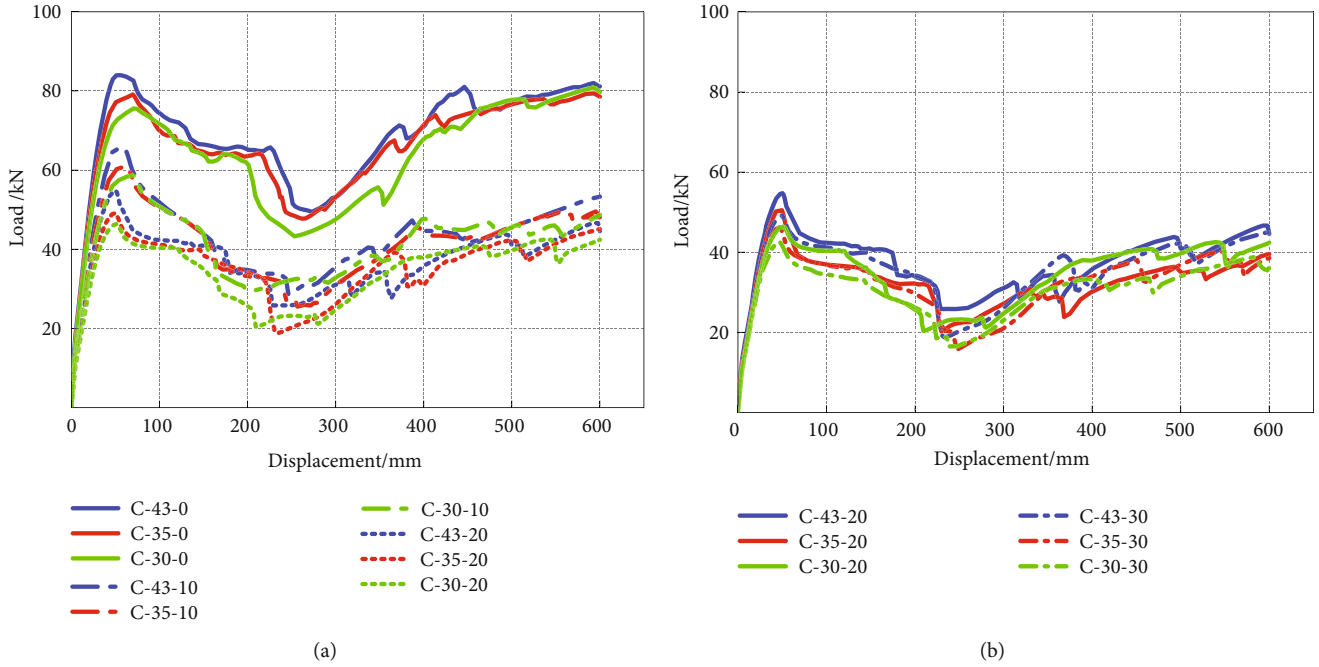
FIGURE 10: Load–displacement curves in span with different concrete strengths with different corrosion rates. (a) Corrosion rate 0、10%、20%. (b) Corrosion rate 20%、30%.

TABLE 5: Peak load and ultimate load of each concrete strength model.

| No. | Peak load $F_p$ (kN) | Displacement corresponding to peak load (mm) | Ultimate load $F_u$ (kN) | Ultimate displacement (mm) | $F_u/F_p$ |
|---|---|---|---|---|---|
| C43-0 | 83.87 | 58.04 | 81.14 | 600 | 0.970 |
| C43-10 | 65.89 | 56.71 | 52.68 | 590 | 0.800 |
| C43-20 | 53.36 | 50.30 | 43.47 | 589 | 0.815 |
| C43-30 | 50.48 | 49.69 | 39.40 | 597 | 0.781 |
| C35-0 | 79.10 | 69.69 | 79.40 | 600 | 1.004 |
| C35-10 | 60.96 | 60.93 | 49.14 | 595 | 0.806 |
| C35-20 | 49.14 | 50.04 | 44.14 | 591 | 0.898 |
| C35-30 | 46.24 | 47.38 | 40.19 | 553 | 0.869 |
| C30-0 | 78.59 | 70.76 | 80.16 | 580.19 | 1.020 |
| C30-10 | 58.57 | 72.10 | 46.04 | 579.70 | 0.786 |
| C30-20 | 47.63 | 67.29 | 40.63 | 579.21 | 0.853 |
| C30-30 | 42.60 | 47.41 | 38.76 | 571.52 | 0.909 |

the corroded rear beam; $n_{bar}$ is the number of single layers of reinforcement in the compression zone; $\omega_{cr}$ is the width of the crack caused by a single reinforcement at an erosion depth of $X$; $v_{rs}$ is the volume expansion rate of corrosion products, which can be taken as 2; and $u_{icorr}$ is the width of a crack.

Corrosion of the reinforcement causes a reduction in the bond between the reinforcement and the concrete, which is accounted for by the bond reduction factor that was previously introduced.

*2.5. Validation of the Model.* Based on the established FE model, a numerical analysis of the resistance of the RC substructure to progressive collapse is carried out, and the valid-

ity of the FE model is verified by comparison with the results of three specimens from literature [12]. In Figure 5, the load–deflection curves and results of the test of the non-corroded beam BS-0, the corroded beam BS-15-5, and the corroded beam BS-30-5 are compared.

For the non-corroded beam, when the displacement reaches 73 mm, the peak value reaches 77.6 kN due to the CAA. The comparable experimental result is 77.2 kN. As the displacement increases, the load decreases. When the displacement reaches 282 mm, the TCA goes into effect and finally reaches its peak value. At that time, the load is 88 kN, which is 2.2% away from the experimental result. During the experiment, the load–deflection curve suddenly
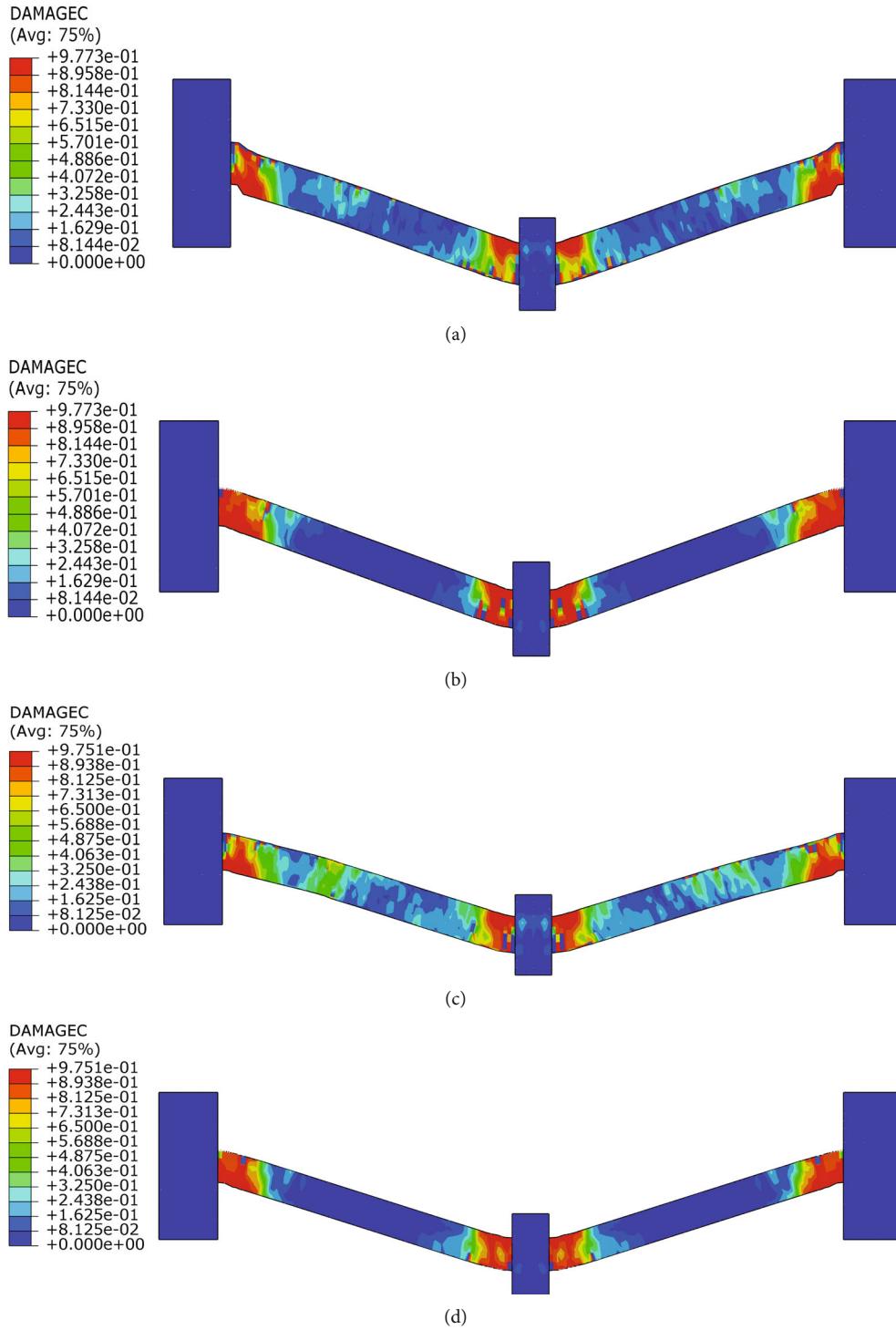
(a)



(b)
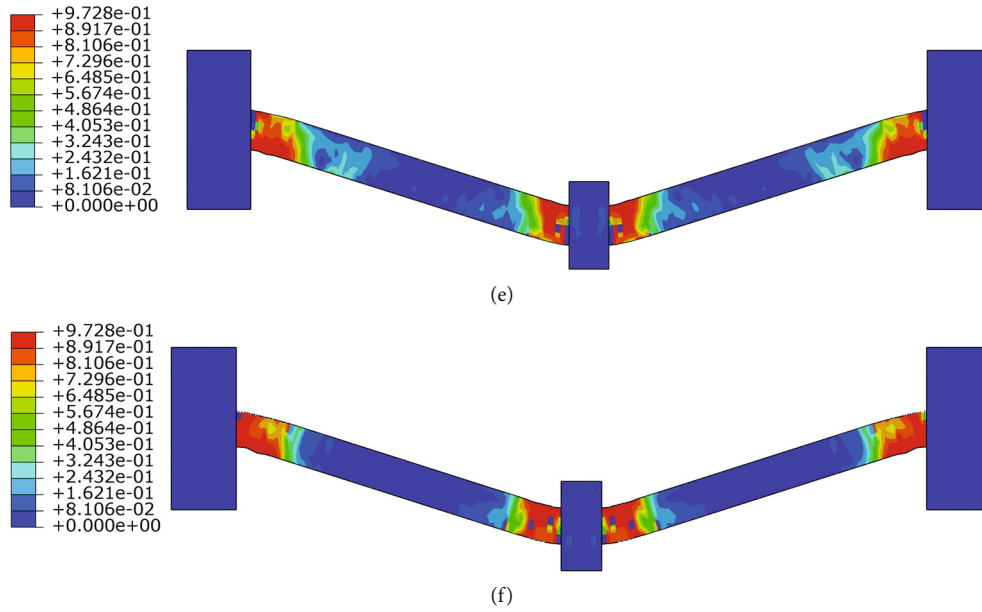


(c)



(d)

Figure 11: Continued.

(e)



(f)

FIGURE 11: Final loss diagram of partial models with different concrete strength grades. (a) C-43-0. (b) C-43-20. (c) C-35-0. (d) C-35-20. (e) C-30-0. (f) C-30-20.
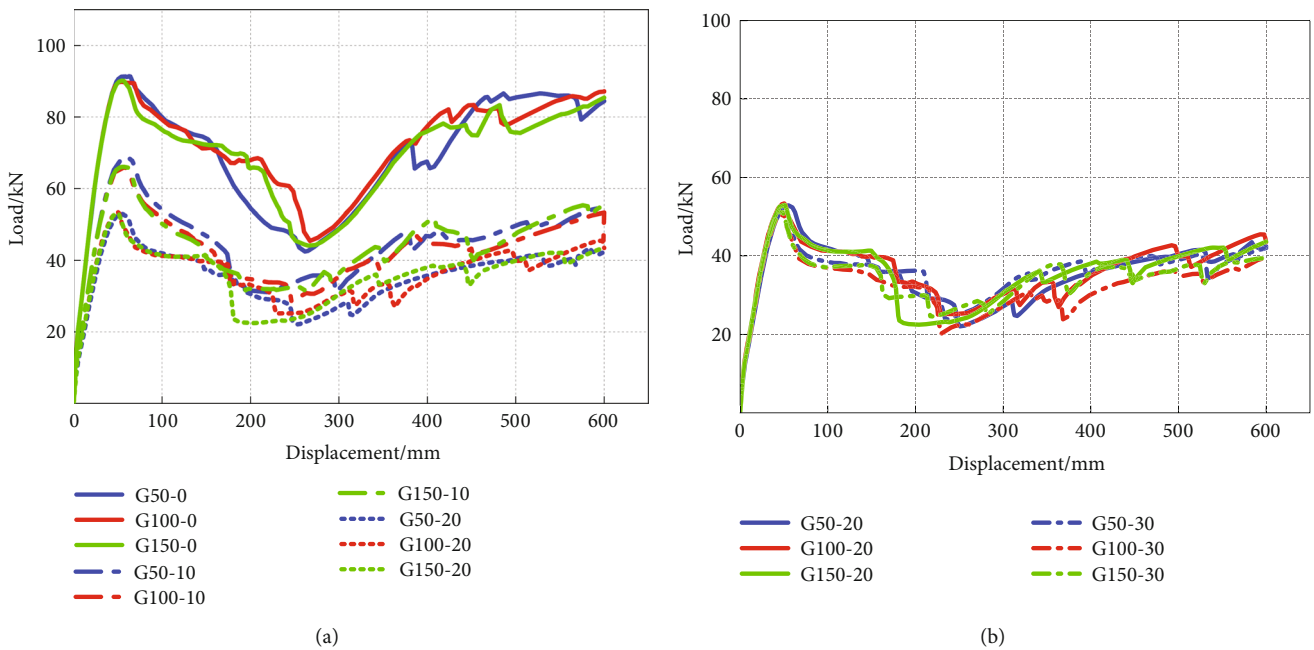


(a)



(b)

FIGURE 12: Mid-span load–displacement curve of different corrosion rates and different stirrup spacing. (a) Corrosion rate 0、10%、20%. (b) Corrosion rate 20%、30%.

drops when the displacement is 329 and 585 mm, which is caused by the fracture of the longitudinal reinforcement. The simulation results of model BS-15-5 and model BS-30-5 are similar, and the relevant data are shown in Table 2.

From Table 2, it can be seen that the FE model predicts the yield load of the members and the peak load under CAA well, but the variability of the ultimate load under TCA is relatively large, especially for the BS-15-5 specimen, where the difference in ultimate load is 22%. This occurs because in the real load, the concrete and reinforcement continue to develop until they stop

working after cracking has occurred, reducing the load-bearing capacity of the specimen. On the contrary, in this model, the failure of the reinforcement and concrete units is not accurately simulated, and the units that should actually fail continue working, leading to an increase in the ultimate load-bearing capacity. However, the FEM can accurately represent the overall tendency of the specimen to resist progressive collapse, which verifies the correctness and applicability of the model. Cracking starts when the sign of the maximum principal plastic strain or the values of the compression equivalent effect

TABLE 6: Peak load and ultimate load of each model with different stirrup spacing.

| Model no. | Peak load $F_y$ (kN) | Displacement corresponding to peak load (mm) | Ultimate load $F_u$ (kN) | Ultimate displacement (mm) | $F_u/F_y$ |
|---|---|---|---|---|---|
| G50-0 | 91.32 | 58.72 | 86.60 | 527 | 0.948 |
| G50-10 | 68.28 | 63.55 | 54.70 | 600 | 0.801 |
| G50-20 | 52.86 | 49.59 | 50.58 | 575 | 0.957 |
| G50-30 | 52.43 | 49.90 | 40.21 | 576 | 0.856 |
| G100-0 | 89.83 | 54.17 | 87.19 | 600 | 0.955 |
| G100-10 | 65.89 | 56.71 | 52.68 | 590 | 0.800 |
| G100-20 | 53.36 | 50.30 | 43.47 | 589 | 0.815 |
| G100-30 | 50.48 | 49.69 | 39.40 | 597 | 0.781 |
| G150-0 | 90.17 | 54.22 | 85.40 | 600 | 0.947 |
| G150-10 | 66.06 | 56.42 | 55.49 | 693 | 0.840 |
| G150-20 | 53.00 | 50.94 | 42.10 | 552 | 0.794 |
| G150-30 | 51.14 | 48.24 | 38.60 | 574 | 0.755 |

variation and tensile are positive [14]. Figures 6, 7, and 8 show that the results of FEM agree with the experimental and fracture mechanisms of the specimen. Based on the crack morphology, the model remains dominated by the bending damage mode, and cracks appear at the maximum bending moment, particularly at the middle and the two ends of the specimen.

Figure 9 shows the comparison of the test horizontal load–displacement relationship curves and FEM results of the BS-0, BS-15-5, and BS-30-5, respectively. It can be observed that the overall trend of the finite element analysis results is basically consistent with the experimental results. However, due to the differences between the actual boundary conditions of the experiment and the simplified boundary conditions of the finite element model, the overall peak value of the finite element model is greater than the experimental results. In the later stage, due to the fracture of the steel bar, the load value undergoes some shaking, but the finite model cannot effectively simulate the fracture effect of the steel bar. Therefore, the error in the later TCA is large. The maximum horizontal pressure of the test piece BS-0 is 202.0 kN when the displacement is 112 mm, while the finite element analysis shows that the maximum pressure of the model is 212 kN when the displacement is 135 mm, with an error of 4.9%. After reaching the TCA, the test results show that the maximum tensile force is 147 kN when the displacement is 553 mm. Through FEM, the maximum tensile force is 212.8 kN when the displacement is 544 mm, and the tensile force conversion point is 286 mm, 2.0% ahead of the experimental value. Table 3 shows the comparison of the horizontal reaction test values and FEM results of the three specimens.

From the above analysis, it can be seen that the finite element analysis results are in good agreement with the test results, but the model cannot simulate the fracture of the reinforcement very well, resulting in a large error in the TCA. On the whole, the finite element model has certain correctness and guidance and can show the characteristics of the test piece in the whole test process.

## 3. Analysis of Progressive Collapse Resistance Mechanism

To study the influence of different design parameters on the progressive collapse resistance of corroded RC substructures, this paper evaluates three key parameters, namely, the concrete strength grade, stirrup spacing, and substructure span–depth ratio. Based on these design parameters, three series of models are designed to control the concrete strength, stirrup spacing, and span–depth ratio of the substructure, which are represented by the letters C, G, and H, respectively. Considering "C35-5" as an example, this nomenclature signifies that the change parameter is concrete, the compressive strength of the concrete cube is 35 MPa, and the mass corrosion rate of the substructure is 5%. We refer to Table 4 for the specific model and parameters used here.

### 3.1. Effect of the Concrete Strength.
The other design conditions are the same except for the change in compressive strength of the concrete cube. Figure 10 shows the midspan load–deflection curve of members with different concrete strengths when the corrosion rate is 0%, 10%, 20%, and 30%. The same lines in the figure represent the same corrosion rates, and the same colors represent the same concrete strengths.

Figure 10 shows that the influence of concrete strength on the performance of the substructure mainly manifests in the beam mechanism and CAA, and the concrete strength grade has a certain promoting effect on the CAA of components. In the TCA of large deformation, the increase in ultimate load of specimens with the same corrosion rate and different concrete strength is not clear, but it can still be seen that the ultimate strength of specimens with higher concrete strength grade is also slightly higher. The main explanation for this phenomenon is that in the FE model, the concrete unit does not stop working after failure but continues to provide a certain tensile strength, which greatly disturbs the ultimate strength.
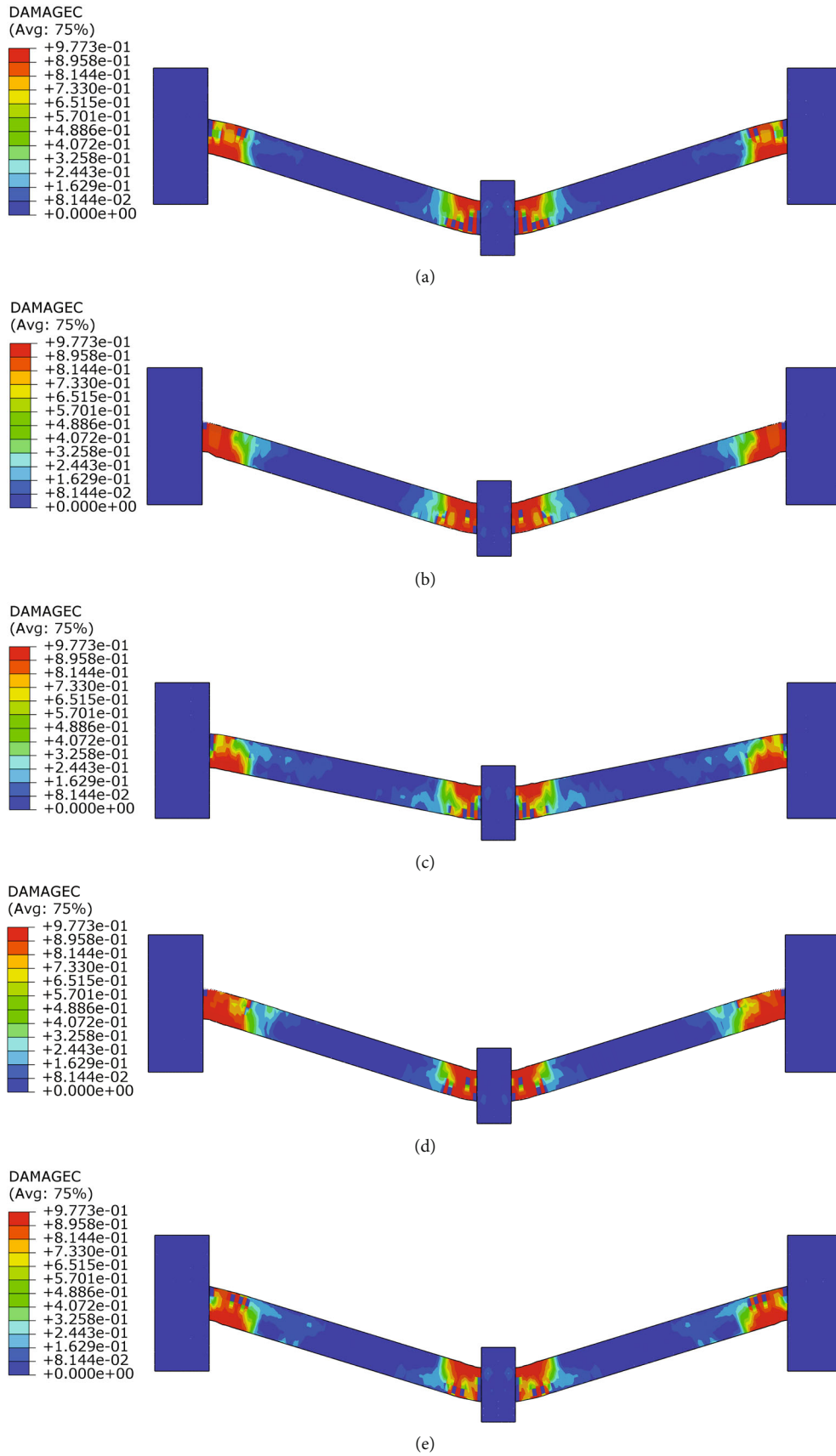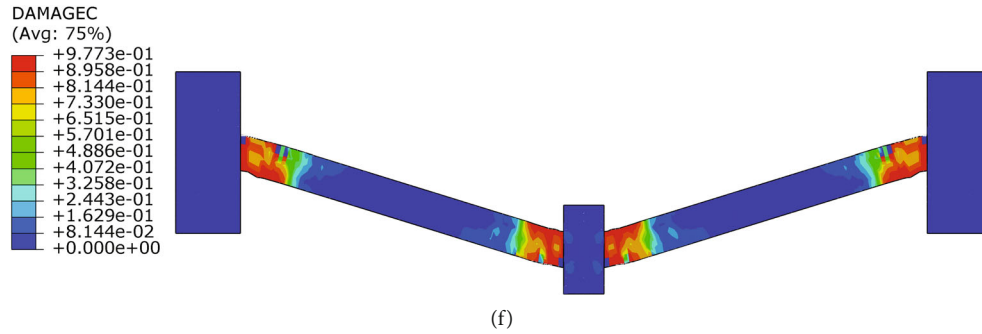
(f)

FIGURE 13: Final loss diagram of models with different stirrup spacing. (a) G-50-0. (b) G-50-20. (c) G-100-0. (d) G-100-20. (e) G-150-0. (f) G-150-20.

The peak load, ultimate load, and displacement of each model in the arch compression stage are shown in Table 5. Compared to specimen "C30-10", the peak values of models "C35-10" and "C43-10" increased by 4.03% and 12.43%, respectively, in CAA and increased by 1.12% and 8.42%, respectively, in large deformation TCA. With the increase in concrete strength, the load corresponding to CAA and TCA at the same corrosion rate has thus improved to a certain extent. Figure 9(a) shows that when the corrosion rate reaches 10%, the decrease trend of the ultimate strength of the model in the large deformation stage slows significantly. Figure 9(b) shows that when the corrosion rate reaches 20%, the decrease speed of the peak load of the CAA of the model slows. When the corrosion rate reaches 20%, the concrete cover has basically withdrawn from load bearing and mainly relies on the compressive effect of the concrete in the core area, the hoop effect due to the continuous reduction of the hoop cross-sectional area, and the strength of the reinforcement member in the CAA. The peak value decreases slowly when the member is in the large deformation stage, such that the member relies mainly on the tensile action of the reinforcement, and the material properties of the reinforcement in the specimen at different rusting rates are the main reason for the influence on its ultimate strength.

Figure 11 lists the final damage states of some of the models from the loss diagram. When rusting occurs, the plastic deformation of the model is increasingly concentrated in the beam–column nodes out, and the plastic deformation in this intermediate region is small.

*3.2. Effect of Stirrup Spacing.* Retaining all other conditions, only the stirrup spacing of the member is changed. The three models, "G50", "G100", and "G150", were used to evaluate the effect of different stirrup spacing on the collapse resistance of beam–column structures under different corrosion rates. Figure 12 shows that the load–deflection curve trend of the three components with different stirrup spacing is basically the same under each corrosion rate, and the peak load of the three models is also basically the same. This shows that the stirrup configuration has no effect on the bearing capacity and deformation resistance of the substructure and has no clear improvement on the degradation after corrosion under the condition of meeting the requirements of the code.

Table 6 shows the peak load and ultimate load of each rust rate state with different hoop spacings. From the data in the table, it can be seen that changing the hoop spacing exhibits little effect on the peak load and ultimate load of the model under meeting the specification requirements, and the peak load and ultimate load of each model decrease with increasing rust rate. In the beam mechanism and the compression arch effect stage, there is a slight difference between the three members because the hoop spacing is different and the restraining effect on the concrete in the core area is also different. For the suspension chain line mechanism, the three curves show approximately the same trend, and the ultimate loads are within the acceptable error range. The difference between the three models exists mostly due to model errors, and the failure of the concrete and reinforcement units occurs without leaving the working region. Figure 12 also shows that the load-bearing capacity of the subcomponent gradually changes from concrete to longitudinal reinforcement when the suspended chain line mechanism occurs, and the role of the hoop reinforcement in the large deformation stage is basically negligible.

The final damage state of some models is shown in Figure 13. As the stirrup spacing decreases, the plastic deformation of the beam becomes increasingly concentrated at the beam–column joints, which is quite detrimental to the ductility development of the beam at the large deformation stage, especially when structural performance degradation, reinforcement corrosion, and other factors occur. There exists no exact safety margin when the structure undergoes large deformation. Therefore, provided that the code requirements are met, it is advantageous to select the appropriate and economical stirrup spacing for the large deformation stage.

*3.3. Effect of Different Substructure Span–Depth Ratio.* The span–depth ratio is next varied by retaining the beam section size constant and varying the beam span. The span–depth ratios of the three members are 14, 16, and 18. It can be seen from the analysis in Figure 14 that the peak load of the model continues to increase as the span–depth ratio decreases, but the TCA of the model becomes increasingly weaker. As the corrosion rate increases, the vertical capacity of each component continues to deteriorate. The smaller the span–depth ratio of the structure is, the higher the peak load
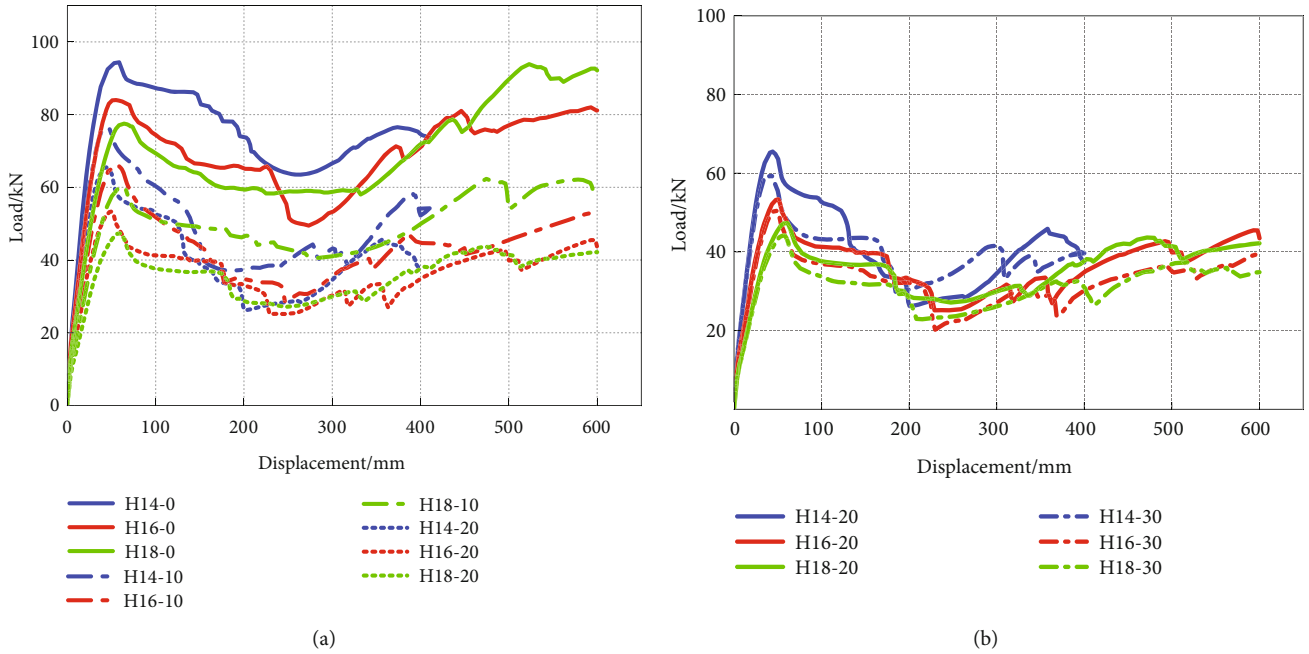
(a)

(b)

FIGURE 14: Mid-span load–displacement curve with different corrosion rate and different span–depth ratio. (a) Corrosion rate 0、10%、20%. (b) Corrosion rate 20%、30%.

TABLE 7: Peak load and ultimate load of models with different span–depth ratios.

| Model no. | Peak load $F_y$ (kN) | Displacement corresponding to peak load (mm) | Ultimate load $F_u$ (kN) | Ultimate displacement (mm) | $F_u/F_y$ |
|---|---|---|---|---|---|
| H18-0 | 77.50 | 64.20 | 93.1 | 600 | 1.201 |
| H18-10 | 60.41 | 60.04 | 62.17 | 584 | 1.029 |
| H18-20 | 47.36 | 47.36 | 42.18 | 564 | 0.891 |
| H18-30 | 44.17 | 44.17 | 37.36 | 518 | 0.846 |
| H16-0 | 83.87 | 58.04 | 81.14 | 600 | 0.970 |
| H16-10 | 65.89 | 56.71 | 52.68 | 590 | 0.800 |
| H16-20 | 53.36 | 50.30 | 43.47 | 589 | 0.815 |
| H16-30 | 50.48 | 49.69 | 39.40 | 597 | 0.781 |
| H14-0 | 90.75 | 64.31 | 75.80 | 391 | 0.835 |
| H14-10 | 76.75 | 46.50 | 54.22 | 410 | 0.706 |
| H14-20 | 65.48 | 44.07 | 45.8 | 358 | 0.699 |
| H14-30 | 58.28 | 43.32 | 41.14 | 400 | 0.706 |

of the member in the beam mechanism and the CAA, and the smaller the deflection corresponding to the peak load and the ultimate load. Changing the span–depth ratio of the member can significantly change the peak load of the member, yet it reduces the ductility of the member and its deformation capacity. With gradual increases in the corrosion rate, the effect of the span–depth ratio on the improvement of the beam mechanism and the CAA decreases proportionally, while the effect on the TCA is basically lost with the increase in the corrosion rate.

Table 7 shows the peak load and ultimate load of the models under different span–height ratios with different rust ratios. The peak loads are fractions of the intact condition, namely 0.69, 0.64, and 0.62, which shows that as the corrosion rate increases, the influence of the span–height ratio on the load carrying capacity of the model gradually decreases. Figure 15 shows the ultimate damage diagram depicting certain models with different span–height ratios under different corrosion rates. The span–height ratio shows little influence on the plastic region of the structure, which is still dominated by the beam–column nodes. As the corrosion rate increases, the plastic deformation area gradually converges to the beam–column nodes. From Table 7, we also find that the deflection corresponding to the ultimate load occurs relatively earlier for the models with smaller span–height ratios, the peak point is reached earlier in both the compressive and tensile phases, and the displacement corresponding to the peak load and the ultimate displacement is smaller.
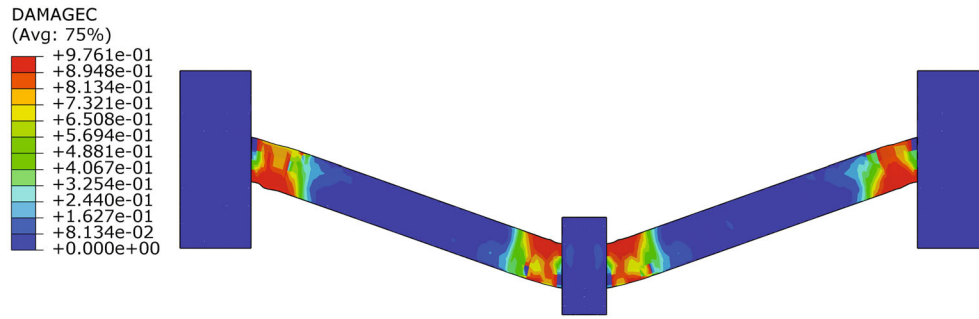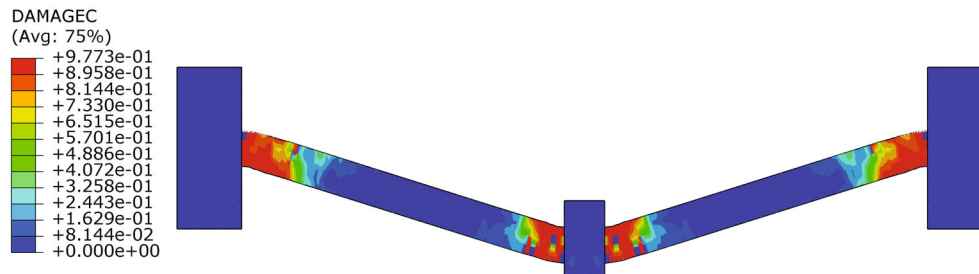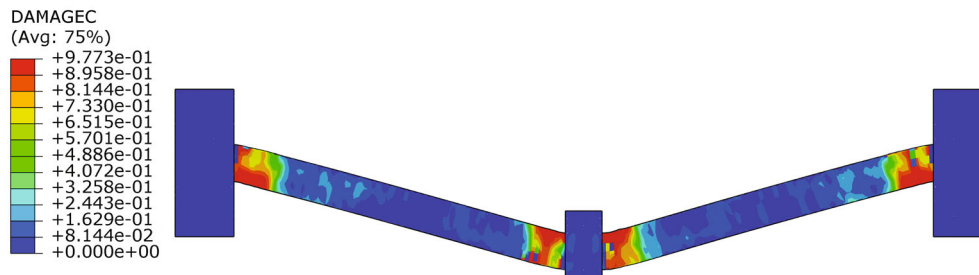
(a)
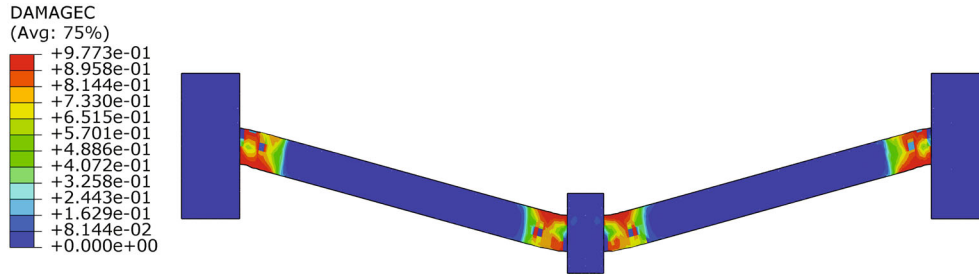
(b)
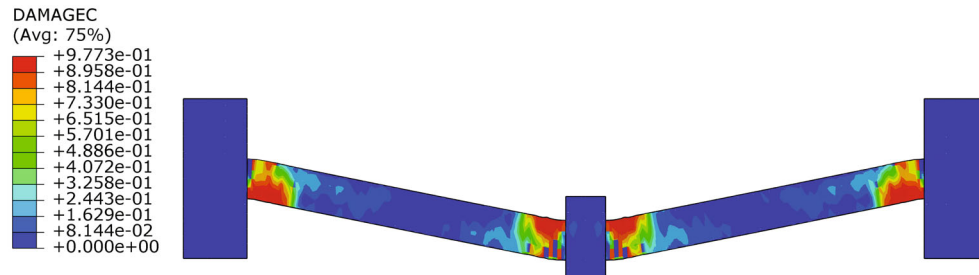
(c)

(d)

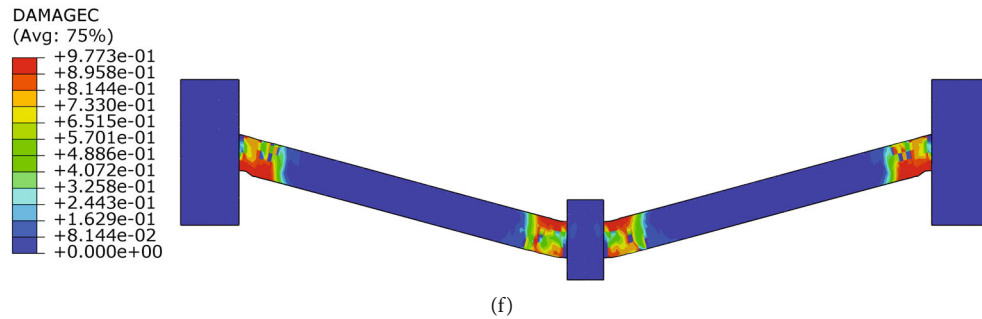(e)

Figure 15: Continued.

(f)

FIGURE 15: Final loss diagram of some models with different span–depth ratios. (a) H-14-0. (b) H-14-20. (c) H-16-0. (d) H-16-20. (e) H-18-0. (f) H-18-20.

*3.4. Brief Summary.* In this section, the influence of concrete strength, stirrup spacing, and specimen span to height ratio on the resistance to continuous collapse is analyzed by changing these parameters. It was found that increasing the strength grade of concrete can slightly increase the peak load of the CAA, but has little effect on the ultimate load during the large deformation stage. Changing the spacing of hoops has little effect on the load-bearing capacity of the structure while meeting the requirements of the specifications. Reducing the span to height ratio of the specimen can significantly increase the peak load of the CAA and the ultimate load during the large deformation stage. However, reducing the span to height ratio of the specimen causes the peak load and ultimate load of the specimen to arrive earlier, and the corresponding displacement is also relatively reduced. The ductility of the specimen is reduced, exhibiting certain brittle characteristics.

## 4. Conclusions

The progressive collapse resistance of RC frame structure considering reinforcement corrosion is investigated, and the main characteristics of the progressive collapse behavior of RC frame beam–column substructures are studied using FEM and theoretical analysis method. The results of this study provide a reference and basis for understanding the performance of RC frame structures with durability damage against progressive collapse. The main conclusions are as follows:

(1) FE simulations of RC frames with reinforcement corrosion can be carried out by considering the bond between reinforcement and concrete, the degradation of reinforcement performance, and the reduction of concrete strength and cross-sectional area, which can accurately predict the development trend of the structure. A model for calculating the load-bearing capacity of peak loads in the CAA stage of beam–column substructures is given at theoretical levels under reasonable assumptions, but there is a lack of corresponding experimental data for further verification.

(2) In the CAA stage of small deformation, increasing the concrete strength can increase the peak load of the CAA, while changing the spacing of the stirrup has minimal effect on the bearing capacity of the CAA stage. The smaller the span–height ratio of the substructure is, the higher the bearing capacity of the CAA stage, and changing the span–height ratio can significantly change the commitment capacity of the member.

(3) In large deformation of the TCA stage, changing the concrete strength has an insignificant effect on the ultimate bearing capacity, but with increases in strength, the bearing capacity increases slightly, while changing the stirrup spacing has a negligible effect on the ultimate bearing capacity. Therefore, the appropriate hoop reinforcement spacing can be selected under the condition of meeting applicable building codes. Increasing the span–height ratio of the member can significantly improve the ultimate bearing capacity and increase the ductility of the structure.

(4) Through the finite element analysis of the RC frame structure, it is found that the peak load and ultimate load of the substructure will be reduced by the reinforcement corrosion. However, after the reinforcement corrosion rate reaches 20%, the impact of the reinforcement corrosion on the bearing capacity of the substructure will be reduced, but at this time, the bearing capacity of the substructure is about 50%–60% of the bearing capacity when it is not corroded, and the bearing capacity can no longer meet the basic use requirements. Therefore, in actual building structures, special attention should be paid to the rust prevention treatment of the structure, and the emphasis on the renovation and reinforcement of old buildings should be increased.

The various investigations of this study are based on the experiments of others and lack of more experimental data to support. In our subsequent work, we are preparing to carry out relevant experimental studies to validate the theoretical model and further investigate the damage mechanism of the RC frame substructure for reinforcement corrosion. More attention should be paid for the long-term service structures especially in corrosive environments, for the reason of the degradation of long-term performance of these structures are more likely to cause serious damage when subjected to extreme events.

## Data Availability

Data supporting this research article are available from the corresponding author or first author on reasonable request.

## Conflicts of Interest

The authors declare that they have no conflicts of interest.

## Authors' Contributions

Chao Bao: conceptualization, methodology, writing—review and editing, and funding acquisition. Dahai Lv: writing—original draft preparation, software, and methodology. Huxiang Wang: visualization and data curation. Yuhang Zhang: software and validation. Xiaotong Ma: project administration and formal analysis. Kar Sing Lim: writing—reviewing and editing. Juping Zhang: supervision.

## Acknowledgments

## References

[1] I. Azim, J. Yang, S. Bhatta, F. Wang, and Q. F. Liu, "Factors influencing the progressive collapse resistance of RC frame structures," *Journal of Building Engineering*, vol. 27, article 100986, 2020.

[2] I. Azim, J. Yang, M. F. Javed et al., "Prediction model for compressive arch action capacity of RC frame structures under column removal scenario using gene expression programming," *Structures*, vol. 25, pp. 212–228, 2020, Elsevier.

[3] X. Long, S. Wang, X. J. Huang, C. Li, and S. B. Kang, "Progressive collapse resistance of exterior reinforced concrete frames and simplified method for catenary action," *Engineering Structures*, vol. 249, article 113316, 2021.

[4] Z. Xi, Z. C. Zhang, W. H. Qin, and P. Zhang, "Experiments and a reverse-curved compressive arch model for the progressive collapse resistance of reinforced concrete frames," *Engineering Failure Analysis*, vol. 135, article 106054, 2022.

[5] J. Yu and K. H. Tan, "Structural behavior of RC beam-column sub-assemblages under a middle column removal scenario," *Journal of Structural Engineering*, vol. 139, no. 2, pp. 233–250, 2013.

[6] I. M. H. Alshaikh, B. H. Abu Bakar, E. A. H. Alwesabi, A. A. Abadel, H. Alghamdi, and M. Wasim, "An experimental study on enhancing progressive collapse resistance using a steel fiber–reinforced concrete frame," *Journal of Structural Engineering*, vol. 148, no. 7, p. 4022087, 2022.

[7] J. X. Wang, Y. J. Shen, S. Gao, and W. D. Wang, "Anti-collapse performance of concrete-filled steel tubular composite frame with assembled tensile steel brace under middle column removal," *Engineering Structures*, vol. 266, article 114635, 2022.

[8] Y. Wang, B. Zhang, X. L. Gu, and F. Lin, "Experimental and numerical investigation on progressive collapse resistance of RC frame structures considering transverse beam and slab effects," *Journal of Building Engineering*, vol. 47, article 103908, 2022.

[9] T. Kiran, N. Anand, M. E. Mathews, B. Kanagaraj, A. D. Andrushia, and E. Lubloy, "G J. Investigation on improving the residual mechanical properties of reinforcement steel and bond strength of concrete exposed to elevated temperature," *Case Studies in Construction Materials*, vol. 16, article e01128, 2022.

[10] Z. Li, Y. Z. Liu, J. S. Huo, and A. Y. Elghazouli, "Experimental and analytical assessment of RC joints with varying reinforcement detailing under push-down loading before and after fires," *Engineering Structures*, vol. 189, pp. 550–564, 2019.

[11] Q. Zhang and Y. Z. Li, "Experimental and modeling study on the progressive collapse resistance of a reinforced concrete frame structure under a middle column removal scenario," *Structural Design of Tall and Special Buildings*, vol. 29, no. 2, article e1693, 2020.

[12] K. Qian, Z. Q. Huang, Y. H. Weng et al., "Study on load carrying mechanism of corroded RC frame structures against progressive collapse," *Journal of Building Engineering*, vol. 43, no. 9, pp. 181–190, 2022.

[13] D. C. Feng, G. Wu, and Y. Lu, "Numerical investigation on the progressive collapse behavior of precast reinforced concrete frame subassemblages," *Journal of Performance of Constructed Facilities*, vol. 32, no. 3, p. 4018027, 2018.

[14] I. M. H. Alshaikh, A. A. Abadel, K. Sennah, M. L. Nehdi, R. Tuladhar, and M. Alamri, "Progressive collapse resistance of RC beam-slab substructures made with rubberized concrete," *Buildings*, vol. 12, no. 10, p. 1724, 2022.

[15] K. Qian, D. Q. Lan, S. K. Li, and F. Fu, "Effects of infill walls on load resistance of multi-story RC frames to mitigate progressive collapse," *Structure*, vol. 33, pp. 2534–2545, 2021.

[16] Y. Li, X. Z. Lu, H. Guan, and P. Ren, "Numerical investigation of progressive collapse resistance of reinforced concrete frames subject to column removals from different stories," *Advances in Structural Engineering*, vol. 19, no. 2, pp. 314–326, 2016.

[17] Z. X. Li, H. K. Liu, Y. C. Shi, and Y. Ding, "Numerical and analytical investigation on progressive collapse resistance of prestressed precast concrete frame structures," *Journal of Building Engineering*, vol. 52, article 104417, 2022.

[18] D. Chang, B. Zeng, L. J. Huang, and Z. Zhou, "Investigation on progressive collapse resistance of prestressed concrete frames with infilled walls," *Engineering Failure Analysis*, vol. 143, article 106866, 2023.

[19] J. Yu, L. Z. Luo, and Y. Li, "Numerical study of progressive collapse resistance of RC beam-slab substructures under perimeter column removal scenarios," *Engineering Structures*, vol. 159, pp. 14–27, 2018.

[20] S. A. E. Kakhki, A. Kheyroddin, and A. Mortezaei, "Evaluation of the progressive collapse of the reinforced concrete frames considering the soil–structure interaction: parametric study based on the sensitivity index," *International Journal of Concrete Structures and Materials*, vol. 16, no. 1, p. 38, 2022.

[21] B. Pang, F. L. Wang, J. Yang, W. Zhang, X. H. Huang, and I. Azim, "Evaluation on the progressive collapse resistance of infilled reinforced concrete frames based on numerical and semi-analytical methods," *Engineering Structures*, vol. 267, article 114684, 2022.

[22] Q. H. Xu, X. Z. Zhen, Y. Zhang, M. Han, and W. Zhang, "Numerical simulation study of progressive collapse of reinforced concrete frames with masonry infill walls under blast

loading," *Modelling and Simulation in Engineering*, vol. 2022, p. 1781416, 2022.

[23] L. Zhang, T. Wei, H. Li, J. Zeng, and X. Deng, "Effects of corrosion on compressive arch action and catenary action of RC frames to resist progressive collapse based on numerical analysis," *Materials*, vol. 14, no. 10, p. 2662, 2021.

[24] D. C. Feng, S. C. Xie, Y. Li, and L. Jin, "Time-dependent reliability-based redundancy assessment of deteriorated RC structures against progressive collapse considering corrosion effect," *Structural Safety*, vol. 89, article 102061, 2021.

[25] I. Fernandez, M. F. Herrador, A. R. Marí, and J. M. Bairán, "Structural effects of steel reinforcement corrosion on statically indeterminate reinforced concrete members," *Materials and Structures*, vol. 49, no. 12, pp. 4959–4973, 2016.

[26] Chinese Standard GB50011-2010, *Code for Seismic Design of Buildings*, pp. 402–404, Building Industry Press of China, Beijing, China, 2016.

[27] H. W. Lin, Y. X. Zhao, J. Ozbolt, P. Feng, C. Jiang, and R. Eligehausen, "Analytical model for the bond stress-slip relationship of deformed bars in normal strength concrete," *Construction and Building Materials*, vol. 198, pp. 570–586, 2019.

[28] H. W. Lin, Y. X. Zhao, J. Q. Yang, P. Feng, J. Ozbolt, and H. Ye, "Effects of the corrosion of main bar and stirrups on the bond behavior of reinforcing steel bar," *Construction and Building Materials*, vol. 225, pp. 13–28, 2019.

[29] Y. L. Hui, Z. S. Lin, and R. Li, "Experimental study and analysis on the property of corroded rebar," *Industrial Building*, vol. 27, no. 6, pp. 11–14+34, 1997.

[30] D. Coronelli and P. Gambarova, "Structural assessment of corroded reinforced concrete beams: modeling guidelines," *Journal of Structural Engineering*, vol. 130, no. 8, pp. 1214–1224, 2004.